Au/Ag Bilayered Metal Mesh as a Si Etching Catalyst for Controlled Fabrication of Si Nanowires

Jungkil Kim,[†,§] Hee Han,[†] Young Heon Kim,[†] Suk-Ho Choi,[§] Jae-Cheon Kim,[†] and Woo Lee[†,‡,*]

[†]Korea Research Institute of Standards and Science (KRISS), Yuseong, 305-340 Daejeon, Korea, [‡]University of Science and Technology (UST), Yuseong, 305-333 Daejeon, Korea, and [§]Department of Applied Physics, Kyung Hee University, Yongin 446-701, Korea

ABSTRACT Au/Ag bilayered metal mesh with arrays of nanoholes were devised as a catalyst for metal-assisted chemical etching of silicon. The present metal catalyst allows us not only to overcome drawbacks involved in conventional Ag-based etching processes, but also to fabricate extended arrays of silicon nanowires (SiNWs) with controlled dimension and density. We demonstrate that SiNWs with different morphologies and axial orientations can be prepared from silicon wafers of a given orientation by controlling the etching conditions. We explored a phenomenological model that explains the evolution of the morphology and axial crystal orientation of SiNWs within the framework of the reaction kinetics.

KEYWORDS: silicon nanowires · metal-assisted chemical etching · Au/Ag bilayered metal mesh · anodic aluminum oxide (AAO) · anodization

Silicon nanowires (SiNWs) have attracted much attention because of their many unique properties and potential applications as building blocks for advanced electronic devices, biological sensors, and optoelectronic devices, as well as for renewable energy devices.[1−6] For both fundamental studies and practical applications of SiNWs, fabrication of ordered arrays of SiNWs with precise control of the location, diameter, length, and density will be of great value. Moreover, it is of utmost importance to synthesize SiNWs with controlled crystal orientations and morphologies because of the close relation between physicochemical properties of SiNWs and their detailed crystal structures, as in many nanostructured low-dimensional materials. Among many fabrication methods, metal-assisted chemical etching (MaCE) has recently attracted considerable attention as a promising alternative SiNW fabrication. In this approach, noble metals (*e.g.*, Ag, Au, Pt, *etc.*) on a silicon substrate are used as catalysts in the chemical etching of silicon with an aqueous solution containing HF and an oxidant (H_2O_2 or metal salts, such as $AgNO_3$, $KAuCl_4$, K_2PtCl_6, $Fe(NO_3)_3$, $Mn(NO_3)_3$).[2−4,6−16] It is generally accepted that a metal acts as a microscopic cathode withdrawing electrons from the underlying silicon (*i.e.*, injection of positive holes (h^+) into silicon) through metal−silicon quasi-Schottky interface, and also as a catalyst for the decomposition or reduction of the oxidants.[11,12] As a result of the microscopic electrochemical process, the silicon that comes in direct contact with a metal undergoes oxidative dissolution in a solution containing HF, maintaining a metal−silicon junction and thus enabling continued movement of the etching front (*i.e.*, metal/silicon interface). Several SiNW fabrication methods employing MaCE have been reported. One of the most intensively utilized methods is wet chemical etching of silicon substrates with a catalyst consisting of interconnected networks of metal nanoparticles (NPs) that can be deposited either by galvanic displacement from a mixture solution containing HF and metal salt or by sputter deposition.[2,3,6−17] However, the resulting SiNWs exhibit poor spatial ordering and broad diameter distribution due to the random two-dimensional (2D) networks of nonuniform metal nanoparticles (see Supporting Information, Figure S1). On the other hand, recent developments have shown that MaCE utilizing metal thin film patterned on a silicon substrate offers several distinct advantages over nanoparticle-based MaCE in terms of control of the location, diameter, spacing, and density of aligned SiNWs.[18−23] Patterning of metal thin films with arrays of nanoholes have been achieved by utilizing polystyrene beads, block copolymers, or ultrathin anodic aluminum oxide (AAO) as patterning masks or by employing laser interference lithography or focused ion beam (FIB) technique.[18−24] However, the reported patterning methods involve complicated processing steps, requiring multiple processes (*e.g.*, sputter deposition of SiO_2, resist removal, oxygen plasma treatment, and

* Address correspondence to woolee@kriss.re.kr.

Received for review January 27, 2011 and accepted March 9, 2011.

Published online March 09, 2011
10.1021/nn2003458

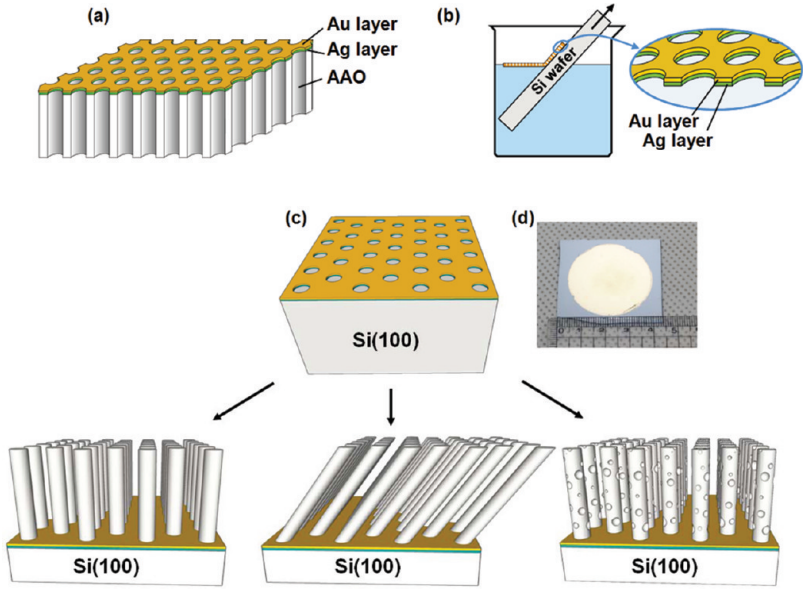

Figure 1. Schematic of the SiNW fabrication process: (a) sequential sputter depositions of Ag and Au on the surface of AAO membrane; (b) transfer of Au/Ag bilayered metal mesh onto a silicon wafer from the surface of etching solution after removal of AAO membrane and also loosely bound metal nanoparticles from the bottom side of the metal mesh; (c) metal-assisted chemical etching (MaCE) of (100)-oriented silicon wafer for the fabrications of SiNWs with controlled axial orientations and morphologies; (d) a photograph of Au/Ag bilayered metal mesh on a Si(100) wafer.

reactive ion etching (RIE)) as well as special techniques for mask preparation. The surfaces of the fabricated SiNWs are often contaminated with numerous metal nanoparticles, which cause porosification of SiNWs due to undesired chemical etching of the wire surface.[19,20] Herein, we report a straightforward and readily accessible method for synthesizing extended arrays of SiNWs with controlled dimensions. Our approach is based on MaCE of silicon wafers by using Au/Ag bilayered metal meshes with arrays of nanoholes that can conveniently be prepared from AAO membranes, overcoming some of the drawbacks involved in conventional MaCE processes using randomly distributed Ag nanoparticles or patterned Ag films. We further show that arrays of SiNWs with different axial orientations and morphologies can be prepared from a silicon wafer of a given orientation by changing the etching parameters. We provide a phenomenological model that explains the evolution of the morphology and axial crystal orientation of SiNWs within the framework of the reaction kinetics.

RESULTS AND DISCUSSION

Au/Ag Bilayered Metal Meshes for Controlled Fabrication of SiNWs. Previously, silver has been popularly employed as a catalyst material for the synthesis of SiNWs arrays by MaCE of silicon because of its superior etching performance over other metal catalysts (*e.g.*, Au, Pt, Cu, or Fe). However, our studies revealed that a silver mesh with regular arrays of nanoholes undergoes dissolution-induced structural failure during silicon etching for an extended period of time or at an elevated etching temperature, which prevents preparation of uniformly aligned SiNWs with controlled diameter and density (see Supporting Information, Figure S2). The problem associated with dissolution of silver metal catalyst becomes serious as the thickness of the patterned silver film decreases. This observation is somewhat in line with the recent reports that silver can be anodically dissolved in an etchant solution containing HF and H_2O_2 (Ag^+/Ag^o, 1.72 V *vs* NHE at pH 0.3), giving rise to surface roughening or porosification of the resulting SiNWs.[6,13,25] In fact, Huang *et al*. reported recently that short SiNWs (aspect ratio = *ca.* 5) prepared by using a patterned thin film of silver have tapered morphologies with different diameters at the top and the bottom part due mainly to the dissolution-induced gradual increase of the hole sizes of silver film during etching even for a short period of time (10−30 s).[19,20] To overcome these problems, we devised a new type of metal mesh with a Au/Ag-stacking configuration, in which the Ag side comes in contact with the polished surface of a silicon wafer during MaCE reaction. Since Au is inert against oxidative dissolution in a mixture solution of HF and H_2O_2, the upper Au layer in our Au/Ag bilayered metal mesh can effectively prevent not only undesired structural disintegration of the underlying Ag layer but also tapering of SiNWs (*vide infra*), still acting as a catalyst for H_2O_2 decomposition on its surface (*i.e.*, $H_2O_2 + 2H^+ + 2e^- \rightarrow 2H_2O$).

The experimental procedure employed in the present work is schematically illustrated in Figure 1. Fifteen nm-thick Ag and 5 nm-thick Au were sequentially sputtered onto an AAO membrane at a deposition rate of 10 nm/min (Figure 1a). The Au/Ag-coated

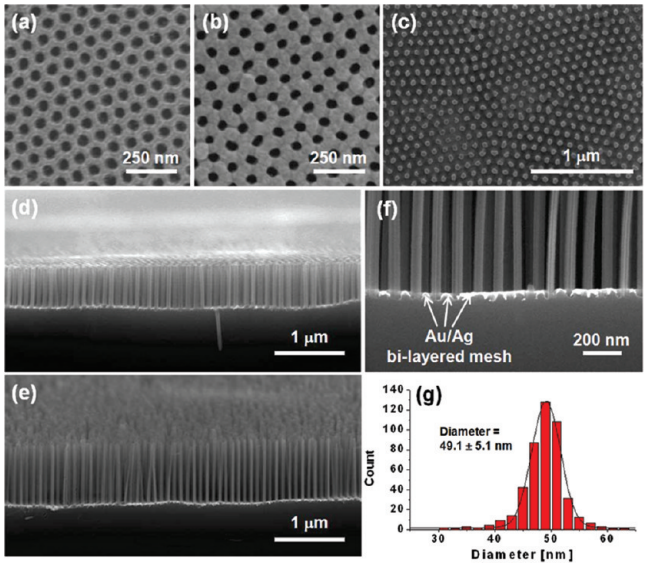

Figure 2. SEM micrographs of (a) AAO membrane and (b) Au/Ag bilayered metal mesh. (c) Typical plan-view SEM image of extended arrays of vertically aligned SiNWs obtained by metal-assisted chemical etching (MaCE) of Si(100) wafers by using Au/Ag bilayered metal mesh. (d,e) Cross-sectional SEM images of vertically etched Si(100) wafers, showing SiNWs with different diameters; (d) 63.9 ± 9.2 and (e) 39.5 ± 4.2 nm. (f) A magnified cross-sectional SEM image of a vertically etched Si(100) wafer taken near the etching front. (g) Histogram showing the diameter distribution of SiNWs shown in panel c, together with a Gaussian fit (solid line) of the measured statistical data.

AAO membrane was floated on the surface of an etching solution (0.1 M NaOH, room temp) to release Au/Ag bilayered metal mesh from the oxide membrane. The resulting metal mesh remained floating on the surface of the aqueous etching solution and could be easily transferred onto any substrates. The edges of nanoholes at the bottom side of the metal mesh were contaminated with loosely connected metal nanoparticles, which were originated from the metal deposited into the pore walls of oxide nanopores during the sputter deposition process. It should be noted that nanometer-sized metal particles participate in the etching reaction during MaCE of a silicon substrate, resulting in SiNWs with irregular surface etch profiles. Therefore, it is recommended to remove the undesired metal nanoparticles from the bottom side of a metal, which can be achieved by floating the sample for about 5 s on a diluted nitric acid solution (10 wt % HNO_3). After removal of metal nanoparticles, nitric acid solution was replaced with deionized water, and finally with a silicon etching solution. The resulting metal mesh was transferred onto a silicon substrate (Figure 1b). Subsequently, the sample was dried to remove the residual amount of silicon etching solution from the interface between the metal mesh and the underlying silicon substrate. The silicon surface contacting with metal was partially etched during the drying step. Since a conformal contact between the metal mesh and the underlying silicon surface was established upon drying, the metal mesh was not separated from the silicon surface even if the sample was exposed to a strong stream of water or nitrogen jet. Fabrication of arrays of SiNWs with controlled morphology and axial orientation could be achieved by immersing metal mesh-loaded silicon wafers (B-doped, resistivity = 1−10 Ωcm) into mixture solutions of HF (46 wt %), H_2O_2 (35 wt %), and H_2O at temperatures ranging from 20 to 70 °C in ambient light (Figure 1c). Our process allowed us to obtain a wrinkle-free metal mesh (diameter = *ca.* 4 cm) on a silicon wafer (Figure 1d), and thus to prepare uniform arrays of epitaxial SiNWs on the entire silicon surface covered with metal mesh.

AAO membranes have been utilized as versatile template materials for fabricating 2D extended arrays of various functional nanostructures due to the unique tailoring capability of the pore size, pore density, pore shape (*e.g.*, circular, square, or triangular pore openings), as well as 2D arrangement of oxide nanopores.[26−29] AAO membranes with a uniform pore diameter in the rage of 20−400 nm and with a pore density in the range of 10^8−10^{10}/cm^2 can conveniently be prepared by anodic oxidation of aluminum.[27] Moreover, oxide nanopores of an as-prepared AAO membrane can be enlarged in a tightly controlled manner *via* a pore wall etching process by using an H_3PO_4 solution.[30] Figure 2 panels a and b display representative scanning electron microscopy (SEM) images of AAO membrane and Au/Ag bilayered metal mesh prepared from it, respectively. The structure of metal mesh is characterized by an ultrathin film perforated by arrays of nanoholes, in which hole array pattern, hole shape, and pitch distance are identical to those of the AAO replication master. It was observed that an average nanohole size of an as-prepared metal mesh is slightly smaller than that of the pore openings of the AAO membrane used for mesh replication. This can be

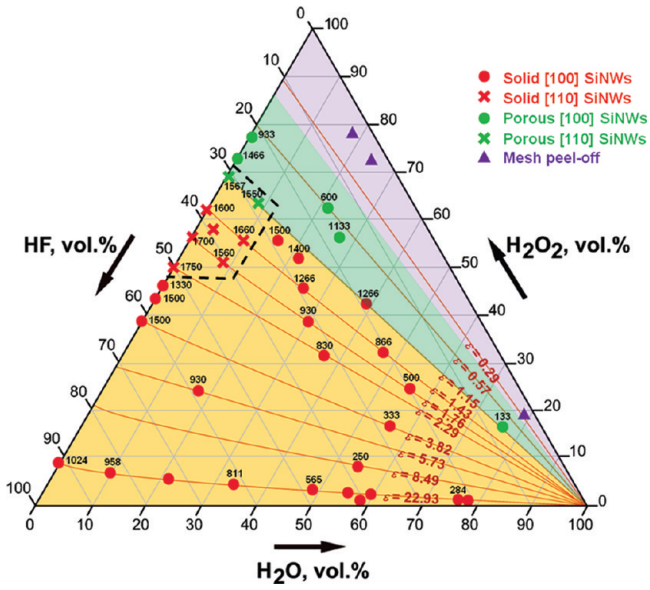

Figure 3. The evolution of etching rate (nm/min), nanowire axial orientation (*i.e.*, etching direction), and morphology during metal-assisted etching of Si(100) wafers in ternary mixtures of 46 wt % HF, 35 wt % H_2O_2, and H_2O at room temperature. The numbers on symbols are the measured etch rates in nm/min. Circle and cross symbols denote experimentally determined axial orientations of SiNWs. Triangle symbols represent experimentally observed peeling-off of catalyst metal mesh from the silicon surfaces. The phenomenon can be attributed to dominant formation of thick oxidized layer over removal of oxidized silicon at low HF and high H_2O_2 concentration.[37] The background areas colored with pale yellow, green, and purple represent the projected etchant conditions, yielding solid nonporous SiNWs, porous SiNWs, and oxidized silicon surface without any etched features due to peeling-off of metal mesh (see Figure S3d), respectively. The region enclosed by dashed line corresponds to the etchant composition window, where etching proceeds along slanted ⟨110⟩ directions to yield [110] SiNWs.

attributed to the progressive decrease of the hole size of metal mesh as a function of deposition time during the metal sputtering process (*i.e.*, the closure effect).[31] Figure 2c−f show typical SEM micrographs of extended arrays of vertically aligned SiNWs fabricated by MaCE of (100)-oriented silicon wafers at room temperature by using Au/Ag bilayered metallic meshes where panel c is the top-view and panels d−f are the cross-section views. Our microscopic investigation indicated that spatial arrangements of nanowires follow exactly the hole array pattern of metal mesh (Figure 2c). To get access to the quantitative information on the size distribution of SiNWs, we performed real-space image analysis on the SEM micrograph shown in Figure 2c by using a standard image processing package (*e.g.*, ImageJ).[32] According to statistical analysis, the mean and standard deviation of the nanowire diameters turned out to be 49.1 ± 5.1 nm (Figure 2g). In the present study, we were able to achieve fine control of the diameter of SiNWs without affecting their separations (*ca.* 100 nm) by taking advantage of the generic tailoring capability of the pore size of the AAO membrane through the pore wall etching process, as demonstrated in Figure 2d (diameter = 63.9 ± 9.2 nm) and Figure 2e (diameter = 39.5 ± 4.2 nm). It should be mentioned that our nanowire samples exhibit fairly uniform etching fronts (*i.e.*, the interface between metal mesh and the underlying silicon substrate), revealing homogeneous metal-assisted etching of silicon without structural failure of catalyst metal mesh (Figure 2d−f). Moreover, individual nanowires have smooth surfaces and uniform diameters along their axes without showing tapered morphology, which can be ascribed to the inert nature of the Au layer of our bilayered metal mesh against anodic dissolution as discussed earlier.

Etching Kinetics *versus* Axial Crystal Orientation and Morphology of SiNWs. In MaCE of silicon wafers, the direction of etching (*i.e.*, the movement direction of catalyst metal) determines the axial crystal orientation of the resulting SiNWs. In the present work, we found that the etching direction of silicon of a given crystal orientation can be changed by altering etching conditions to yield arrays of SiNWs with different axial orientations. As in the electrochemical etching of silicon, etching direction in MaCE has known to be mainly dependent on the crystallographic orientation of starting silicon wafers with preferred etching along the ⟨100⟩ directions.[12,33−35] On the other hand, it was reported recently that etching direction is mainly determined by the molar ratio of HF to H_2O_2 (*i.e.*, ε = [HF]/[H_2O_2]) irrespective of crystal orientations of the starting silicon wafers.[14,24] However, the results in literature are rather conflicting, and the origin of different etching behaviors remains to be further explored for controlled fabrication of aligned SiNWs with defined axial orientations. We found that the evolution of etching directions should be understood in terms of reaction kinetics involved in MaCE of silicon, rather than just simple considerations on the concentration ratio (ε) of HF to H_2O_2, as we will discuss in detail below.

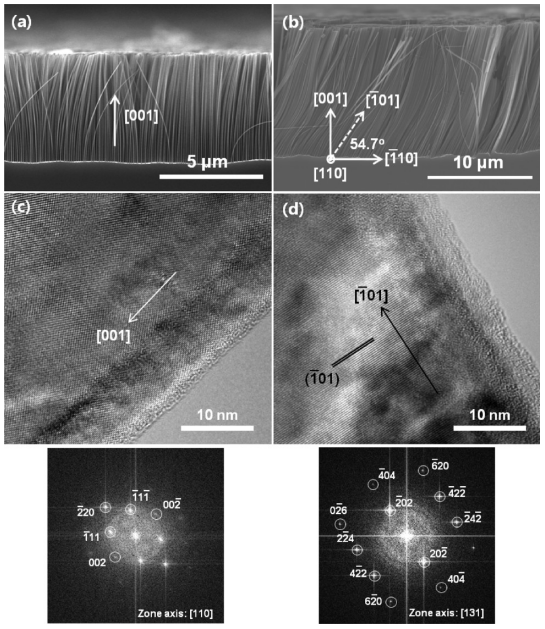

Figure 4. Representative cross-sectional SEM micrographs of SiNWs formed by (a) vertical and (b) slanted etching of Si(100) wafers. (c,d) High-resolution transmission microscopy (HRTEM) images of SiNWs taken from the samples shown in panels a and b, respectively. The corresponding fast Fourier transform (FFT) patterns of HRTEM images in panels c and d are displayed below the respective panels, from which the directions of etching were confirmed to be ⟨100⟩ and ⟨110⟩ for the samples shown in panels a and b, respectively. Note that, in a Si(100) wafer, fracture occurs preferentially along ⟨110⟩ directions.[41] Accordingly, viewed from [110] axis, SiNWs formed by [$\bar{1}$01] etching appear to be tiled by 54.7° with respect to the wafer surface (although they are actually tiled by 45°), as denoted by the dashed arrow in panel b.

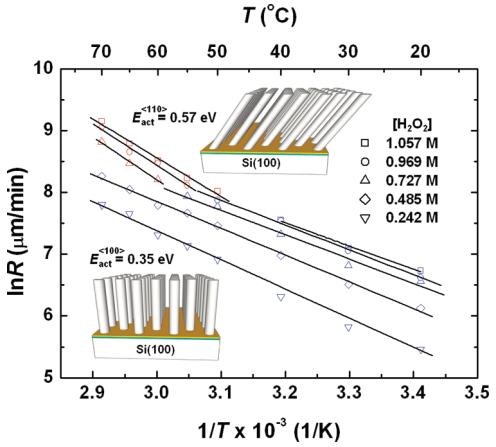

Figure 5. Arrhenius plots showing the temperature dependence of the etching rates (ln(rate) *vs* 1/*T*) for metal-assisted etching of (100)-oriented silicon wafers by using etchant solutions with different compositions, in which the concentration of H_2O_2 was varied in the range 0.242−1.057 M by controlling the amount of water, while the molar ratio of HF to H_2O_2 was fixed to ε = 22.931. Blue symbols represent experimentally measured rates of etching along the vertical ⟨100⟩ direction, while red ones represent rates of etching along the slanted ⟨110⟩ directions. The solid lines represent the best fits to the experimental data.

Figure 3 shows the evolution of etching rate (in nm/min), etching direction (*i.e.*, nanowire axial orientation), and morphology (solid nonporous *vs* porous) of SiNWs during MaCE of Si(100) wafers in ternary mixtures of HF, H_2O_2, and H_2O at room temperature. Each red line in the present ternary diagram represents the solution composition of the same molar ratio (ε) of HF to H_2O_2. Experimentally observed vertical etchings and slanted ones are marked with circle and cross symbols, respectively. The numbers on symbols are the measured etch rates in nm/min. The vertical etchings are defined as the movement of the etching front perpendicular to the wafer surface, resulting in [100] SiNWs. On the other hand, the slanted etchings are defined as those proceeding in inclined directions (tilted by 45°) with respect to the surface normal, resulting in [110] SiNWs. Under our experimental conditions, we could not observe etching along the ⟨111⟩ directions that are tilted by 35.3° from the wafer surface (*i.e.*, (100) plane). Representative electron micrographs of SiNWs obtained from a vertical ⟨100⟩ etching and a slanted ⟨110⟩ one are shown in Figure 4. Contrary to the recent reports,[14,24] one may see from Figure 3 that there is no correlation between the etching direction and the concentration ratio (ε) of HF to H_2O_2, although the latter appears to affect the morphology of the resulting SiNWs (*i.e.*, solid nonporous SiNWs at $\varepsilon \geq 1.15$ and porous SiNWs at $0.3 < \varepsilon \leq 1.15$; see Figure S3 for morphologies of silicon nanostructures formed at $\varepsilon < 1.15$). It turned out that etchings along slanted ⟨110⟩ directions occur within a narrow window of solution composition, giving high etching rates (the region enclosed by dashed line in Figure 3). It appears that etching direction is mainly dictated by the etching rate, that is, etching occurs along vertical ⟨100⟩ directions at low etching rates, while occurring along slanted ⟨110⟩ directions at high etching rates.

In MaCE of silicon, the movement of the etching front (*i.e.*, metal/silicon interface) is a net consequence of the following two competing events; injection of a positive hole (h^+) into bulk silicon through the metal−silicon quasi-Schottky interface (a process accompanying partial oxidation of silicon) and removal of oxidized silicon by HF from just underneath the catalyst metal. Therefore, the overall etching rate would be governed by the interplay between these two processes. Since the generation of holes (h^+) is related to the catalytic decomposition of H_2O_2 at the interface between the bulk electrolyte and the catalyst metal surface, the amount of holes (h^+) injected into silicon is proportional to the H_2O_2 concentration or its decomposition activity which increases with temperature (*vide infra*). On the other hand, removal of oxidized silicon by HF is associated with the cleavage of its back bonds,[36] of which effective number density in different crystal planes increases with the order {100} < {110} <

{111} (see Supporting Information, Table S1). Under solution conditions ensuring ready removal of oxidized silicon (*i.e.*, etching solutions with high [HF]), catalytic decomposition of H_2O_2 would become the rate determining process. In other words, the etching rate is proportional to the amount of positive holes (h^+) injected into silicon (*i.e.*, reaction rate $\propto$ [H_2O_2]), and the following etching behaviors will operate: At low H_2O_2 concentration, hole (h^+) injection into silicon atoms will be localized at the (100) plane, where there are the fewest silicon back bonds to break, resulting in etching along the ⟨100⟩ direction. As the concentration of H_2O_2 increases sufficiently and thereby the amount of the generated holes (h^+) exceeds a certain threshold, removal of silicon atoms would occur with great rapidity in the crystal planes, where there are more silicon back bonds to polarize, resulting in ⟨110⟩ and even possibly ⟨111⟩ etchings. Analogously, the following etching behaviors will operate for the solution conditions ensuring a large generation of positive holes (h^+) (*i.e.*, etching solutions with high [H_2O_2]), in which removal of oxidized silicon by HF governs overall etching reaction (*i.e.*, reaction rate $\propto$ [HF]) and also etching direction: At low HF concentration, removal of oxidized silicon will take place slowly in the least compact (100) plane due to limited amount of HF. In the mean time, an extra amount of injected holes (h^+) can readily diffuse away from the etching front to lattice defects and dopant sites (pore nucleation sites) on the surface of the already formed SiNWs,[3,11,37−39] resulting in porous [100] SiNWs. At high HF concentration, on the other hand, removal of oxidized silicon would be kinetically favored in the crystal planes with a higher density of silicon back bonds, resulting in etchings along non-⟨100⟩ directions. Porous nanowire morphology may emerge, if there are extra holes (h^+) that are not consumed completely at the etching front. In other words, both high H_2O_2 concentration for large generation of positive holes (h^+) and low HF concentration for limited removal of oxidized silicon are the necessary condition for porous nanowire formation (*i.e.*, etching solutions with low [HF]/[H_2O_2] ratio, ε).

Etching Directions *versus* Activation Energies. The present kinetic relevance of the etching directions could be corroborated by demonstrating that MaCE of Si(100) wafers with etching solutions of a fixed [HF]/[H_2O_2] ratio (ε = 22.931) can result in switching of the etching direction from vertical ⟨100⟩ at room temperature to slanted ⟨110⟩ at elevated temperature. Since decomposition activity of H_2O_2 on the surface of catalyst metal increases with temperature,[40] hole (h^+) injection into silicon can be promoted at an elevated temperature. Correspondingly, temperature positively correlates with the etching rate, provided that HF is readily available (*i.e.*, high [HF]). Figure 5 shows the temperature dependence of the etching rates (*i.e.*, Arrhenius plots; $\ln(R) = \ln(A) - E_a/(k_BT)$, where R is the etching rate, A is the pre-exponential (frequency) factor, E_a is the activation energy for etching, and k_B is the Boltzmann constant-). Etched in solutions with [H_2O_2] $\leq$ 0.485 M, etching proceeded always along the vertical ⟨100⟩ direction even though the temperature was varied from 20 to 70 °C. In contrast, for etchant solutions with [H_2O_2] $\geq$ 0.727 M, switching of the etching direction from vertical ⟨100⟩ to slanted ⟨110⟩ took place at an elevated temperature. Upon closer examination of the present kinetic plots, one may see that the switching temperature decreases with increase in H_2O_2 concentration, and switching of the etching direction is accompanied by changes of the slopes. According to our analysis, averaged activation energy for ⟨110⟩ etching turned out to be higher than that for ⟨100⟩ etching; $E_a^{\langle 110\rangle} = 0.57 \pm 0.03$ eV and $E_a^{\langle 100\rangle} = 0.35 \pm 0.05$ eV. The activation energy for etching corresponds to the energy barrier for displacing a silicon atom from its site. We attribute the observed higher activation energy for ⟨110⟩ etching to higher density of silicon back bonds in (110) plane compared to the (100) one. On the other hand, the observed H_2O_2 concentration dependence of the switching temperature strongly implies that there is a threshold amount of the positive holes (h^+). Above the threshold, weakening of silicon back bonds in the (110) plane may occur effectively. Below the threshold, however, hole injection will be limited to the silicon atoms in the (100) plane resulting in etching along the ⟨100⟩ direction, even if the etching rate is high enough due to increased reaction temperature. We propose here that etching along the non-⟨100⟩ directions occurs only if the etching condition can guarantee both the generation of a large amount of positive holes (h^+) and the fast removal of oxidized silicon by HF (*i.e.*, a condition satisfying fast etching reaction). Although we mainly discussed the evolution of the morphology and axial orientation of SiNWs during MaCE of Si(100) wafers, our preliminary results indicate that the arguments made above can be generally applied to non-(100)-oriented Si wafers.

CONCLUSION

We developed Au/Ag bilayered metal meshes with regular hexagonal arrays of nanoholes as a catalyst for wet-chemical etching of silicon. The newly developed etching catalyst allows us not only to overcome drawbacks involved in conventional Ag-based silicon etching processes, but also to fabricate arrays of uniform silicon nanowires. We demonstrated that SiNWs with different axial orientations and morphologies can be prepared from a silicon wafer of a given orientation by deliberately controlling the etching conditions. Our

results revealed that reaction kinetics has profound implication for the evolution of morphology and axial orientation of SiNWs during metal-assisted chemical etching of silicon.

METHODS

Membrane Preparation. Free-standing self-ordered nanoporous anodic aluminum oxide (AAO) membrane was prepared by anodization of aluminum as follow: As-received aluminum discs (Goodfellow, 99.999%) were used in anodization experiments without the annealing step. On the other hand, the aluminum discs were electrochemically polished in an 1:4 mixture solution of 65% $HClO_4$ and 99.5% ethanol (5 °C) in order to exclude, if any, potential side effects (*e.g.*, localized field concentration) that could arise from the surface roughness during anodization. A surface finished aluminum disk was placed in an electrochemical cell with an O-ring, so that one side of metal could be anodized. Anodization was conducted under a regulated cell voltage of 40 V using 0.3 M $H_2C_2O_4$ (5 °C) as an electrolyte for 15 h. Anodization of aluminum in the present work was performed by using an electrochemical cell equipped with a cooling stage that is in thermal contact with the aluminum substrate to remove the reaction heat.[26] After anodization, the remaining Al substrate was selectively removed by using a mixture solution containing 3.4 g $CuCl_2 \cdot 2H_2O$, 50 mL of 38 wt % HCl, and 100 mL of DI water. The bottom surface of AAO that originally came in contact with the aluminum substrate is sealed by a *ca.* 46 nm-thick barrier oxide layer. This barrier oxide layer was removed by exposing the bottom surface of AAO to 5 wt % H_3PO_4 (30 °C) for 30 min to obtain a through-channel membrane.

Pretreatment of Si Wafers. A set amount of (100)-oriented *p*-Si wafers (B-doped, $\rho = 1-10$ Ωcm) were cleaned by using either a RCA solution ($NH_3 \cdot H_2O/H_2O_2/H_2O$, v/v/v = 1/1/5) or a Piranha solution (98% H_2SO_4/30% H_2O_2, v/v = 4/1) and then thoroughly rinsed by copious amounts of deionized (DI) water prior to use.

Microscopic Characterization. A Hitachi S-4800 field emission scanning electron microscope (FE-SEM) was employed for the morphological characterization of the samples. The samples were mechanically cleaved for the cross-sectional SEM investigations. The crystallographic orientation of the SiNWs were investigated by a transmission electron microscope (TEM, Tecnai F30, FEI, USA) operated at a primary beam energy of 300 kV. To prepare specimens for TEM investigation, the surface of an etched Si substrate was scraped using a razor blade, and SiNWs in the scrapings were collected and dispersed in absolute ethanol. A drop of the resulting suspension solution was placed on a carbon-coated Cu grid.

Acknowledgment. This research was supported by Future-based Technology Development Program (Nano Fields) through the National Research Foundation of Korea (NRF) funded by the Ministry of Education, Science and Technology (Grant No. 2010-0029332), and in part by Korea Research Council of Fundamental Science and Technology (KRCF) through the KRISS project of "Development of Advanced Industrial Metrology".

Supporting Information Available: SEM micrographs of SiNWs fabricated with randomly distributed silver nanoparticles and silver mesh with arrays of nanoholes; SEM micrographs of silicon nanostructures formed at $\varepsilon < 1.15$; table showing the relationship among surface bond orientation, atomic arrangement, and silicon back-bond density for Si(100), Si(110), and Si(111) planes. This material is available free of charge *via* the Internet at http://pubs.acs.org.

REFERENCES AND NOTES

1. Chan, C. K.; Peng, H.; Liu, G.; McIlwrath, K.; Zhang, X. F.; Huggins, R. A.; Cui, Y. High-Performance Lithium Battery Anodes Using Silicon Nanowires. *Nat. Nanotechnol.* **2008,** *3*, 31–35.
2. Hochbaum, A. I.; Chen, R.; Delgado, R. D.; Liang, W.; Carnett, E. C.; Najarian, M.; Majumdar, A.; Yang, P. Enhanced Thermoelectric Performance of Rough Silicon Nanowires. *Nature* **2008,** *451*, 163–167.
3. Hochbaum, A. I.; Gargas, D.; Hwang, Y. J.; Yang, P. Single Crystalline Mesoporous Silicon Nanowires. *Nano Lett.* **2009,** *9*, 3550–3554.
4. Kelzenberg, M. D.; Boettcher, S. W.; Petykiewicz, J. A.; Turner-Evans, D. B.; Putnam, M. C.; Warren, E. L.; Spurgeon, J. M.; Briggs, R. M.; Lewis, N. S.; Atwater, H. A. Enhanced Absorption and Carrier Collection in Si Wire Arrays for Photovoltaic Applications. *Nat. Mater.* **2010,** *9*, 239–244.
5. Park, M.-H.; Kim, M. G.; Joo, J.; Kim, K.; Kim, J.; Ahn, S.; Cui, Y.; Cho, J. Silicon Nanotube Battery Anodes. *Nano Lett.* **2009,** *9*, 3844–3847.
6. Qu, Y.; Liao, L.; Li, Y.; Zhang, H.; Huang, Y. Electrically Conductive and Optically Active Porous Silicon Nanowires. *Nano Lett.* **2009,** *9*, 4539–4543.
7. Peng, K.; Wu, Y.; Fang, H.; Zhong, X.; Xu, Y.; Zhu, J. Uniform, Axial-Orientation Alignment of One-Dimensional Single-Crystal Silicon Nanostructure Arrays. *Angew. Chem., Int. Ed.* **2005,** *44*, 2737–2742.
8. Peng, K.; Fang, H.; Hu, J.; Wu, Y.; Zhu, J.; Yan, Y.; Lee, S. T. Metal-Particle-Induced, Highly Localized Site-Specific Etching of Si and Formation of Single-Crystalline Si Nanowires in Aqueous Fluoride Solution. *Chem.—Eur. J.* **2006,** *12*, 7942–7947.
9. Peng, K.; Hu, J.; Yan, Y.; Wu, Y.; Fang, H.; Xu, Y.; Lee, S. T.; Zhu, J. Fabrication of Single-Crystalline Silicon Nanowires by Scratching a Silicon Surface with Catalytic Metal Particles. *Adv. Funct. Mater.* **2006,** *16*, 387–394.
10. Fang, H.; Wu, Y.; Zhao, J.; Zhu, J. Silver Catalysis in the Fabrication of Silicon Nanowire Arrays. *Nanotechnology* **2006,** *17*, 3768–3774.
11. Li, X.; Bohn, P. W. Metal-Assisted Chemical Etching in HF/H_2O_2 Produces Porous Silicon. *Appl. Phys. Lett.* **2000,** *77*, 2572–2574.
12. Peng, K.; Lu, A.; Zhang, R.; Lee, S.-T. Motility of Metal Nanoparticles in Silicon and Induced Anisotropic Silicon Etching. *Adv. Funct. Mater.* **2008,** *18*, 3026–3035.
13. Zhang, M.-L.; Peng, K.-Q.; Fan, X.; Jie, J.-S.; Zhang, R.-Q.; Lee, S.-T.; Wong, N.-B. Preparation of Large-Area Uniform Silicon Nanowires Arrays Through Metal-Assisted Chemical Etching. *J. Phys. Chem. C* **2008,** *112*, 4444–4450.
14. Huang, Z.; Shimizu, T.; Senz, S.; Zhag, Z.; Geyer, N.; Gösele, U. Oxidation Rate Effect on the Direction of Metal-Assisted Chemical and Electrochemical Etching of Silicon. *J. Phys. Chem. C* **2010,** *114*, 10683–10690.
15. Peng, K.-Q.; Yan, Y.-J.; Gao, S.-P.; Zhu, J. Synthesis of Large-Area Silicon Nanowire Arrays *via* Self-Assembling Nanoelectrochemistry. *Adv. Mater.* **2000,** *14*, 1164–1167.
16. Peng, K.; Xu, Y.; Wu, Y.; Yan, Y.; Lee, S.-T.; Zhu, J. Aligned Single-Crystalline Si Nanowire Arrays for Photovoltaic Applications. *Small* **2005,** *1*, 1062–1067.
17. Chen, H.; Wang, H.; Zhang, X.-H.; Lee, C.-S.; Lee, S.-T. Wafer-Scale Synthesis of Single-Crystal Zigzag Silicon Nanowire Arrays with Controlled Turning Angle. *Nano Lett.* **2010,** *10*, 864–868.
18. Huang, Z.; Fang, H.; Zhu, J. Fabrication of Silicon Nanowire Arrays with Controlled Diameter, Length, and Density. *Adv. Mater.* **2007,** *19*, 744–748.
19. Huang, Z.; Shimizu, T.; Senz, S.; Zhang, Z.; Zhang, X.; Lee, W.; Geyer, N.; Gösele, U. Ordered Arrays of Vertically Aligned [110] Silicon Nanowires by Suppressing the Crystallographically Preferred ⟨100⟩ Etching Directions. *Nano Lett.* **2009,** *9*, 2519–2525.

20. Huang, Z.; Zhang, X.; Reiche, M.; Liu, L.; Lee, W.; Shimizu, T.; Senz, S.; Gösele, U. Extended Arrays of Vertically Aligned Sub-10 nm Diameter [100] Si Nanowires by Metal-Assisted Chemical Etching. *Nano Lett.* **2008,** *8*, 3046–3051.
21. Chang, S.-W.; Chuang, V. P.; Boles, S. T.; Ross, C. A.; Thompson, C. V. Densely Packed Arrays of Ultra-High-Aspect-Ratio Silicon Nanowires Fabricated Using Block-Copolymer Lithography and Metal-Assisted Etching. *Adv. Funct. Mater.* **2009,** *19*, 2495–2500.
22. Huang, J.; Chiam, S. Y.; Tan, H. H.; Wang, S.; Chim, W. K. Fabrication of Silicon Nanowires with Precise Diameter Control Using Metal Nanodot Arrays as a Hard Mask Blocking Material in Chemical Etching. *Chem. Mater.* **2010,** *22*, 4111–4116.
23. de Boor, J.; Geyer, N.; Wittemann, J. V.; Gösele, U.; Schmidt, V. Sub-100 nm Silicon Nanowires by Laser Interference Lithography and Metal-Assisted Etching. *Nanotechnology* **2010,** *21*, 095302.
24. Chern, W.; Hsu, K.; Chun, I. S.; Azeredo, B. P. d.; Ahmed, N.; Kim, K.-H.; Zhu, J.-m.; Fang, N.; Ferreira, P.; Li, X. Nonlithographic Patterning and Metal-Assisted Chemical Etching for Manufacturing of Tunable Light-Emitting Silicon Nanowire Arrays. *Nano Lett.* **2010,** *10*, 1582–1588.
25. Lee, C.-L.; Tsujino, K.; Kanda, Y.; Ikeda, S.; Matsumura, M. Pore Formation in Silicon by Wet Etching Using Micrometre-Sized Metal Particles as Catalysts. *J. Mater. Chem.* **2008,** *18*, 1015–1020.
26. Lee, W.; Ji, R.; Gösele, U.; Nielsch, K. Fast Fabrication of Long-Range Ordered Porous Alumina Membranes by Hard Anodization. *Nat. Mater.* **2006,** *5*, 741–747.
27. Lee, W. The Anodization of Aluminum for Nanotechnology Applications. *J. Miner., Metal, Mater Soc.* **2010,** *62*, 57–63.
28. Masuda, H.; Asoh, H.; Watanabe, M.; Nishio, K.; Nakao, M.; Tamamura, T. Square and Triangular Nanohole Array Architectures in Anodic Alumina. *Adv. Mater.* **2001,** *13*, 189–192.
29. Lee, W.; Ji, R.; Ross, C. A.; Gösele, U.; Nielsch, K. Wafer-Scale Ni Imprint Stamps for Porous Alumina Membranes Based on Interference Lithography. *Small* **2006,** *2*, 978–982.
30. Han, C. Y.; Willing, G. A.; Xiao, Z.; Wang, H. H. Control of the Anodic Aluminum Oxide Barrier Layer Opening Process by Wet Chemical Etching. *Langmuir* **2007,** *23*, 1564–1568.
31. Lei, Y.; Chim, W.-K. Shape and Size Control of Regularly Arrayed Nanodots Fabricated Using Ultrathin Alumina Masks. *Chem. Mater.* **2005,** *17*, 580–585.
32. Rasband, W. *ImageJ (public domain)*; NIH: Washington DC, 2006; Vol. 1.36b, http://rsb.info.nih.gov/ij/.
33. Chen, C.-Y.; Wu, C.-S.; Chou, C.-J.; Yen, T.-J. Morphological Control of Single-Crystalline Silicon Nanowire Arrays Near Room Temperature. *Adv. Mater.* **2008,** *20*, 3811–3815.
34. Christophersen, M.; Carstensen, J.; Rönnebeck, S.; Jäger, C.; Jäger, W.; Föll, H. Crystal Orientation Dependence and Anisotropic Properties of Macropore Formation of p- and n-Type Silicon. *J. Electrochem. Soc.* **2001,** *148*, E267–E275.
35. Lehmann, V. The Physics of Macropore Formation in Low Doped n-Type Silicon. *J. Electrochem. Soc.* **1993,** *140*, 2836–2843.
36. Smith, R. L.; Collins, S. D. Porous Silicon Formation Mechanisms. *J. Appl. Phys.* **1992,** *71*, R1–R22.
37. Chartier, C.; Bastide, S.; Lévy-Clément, C. Metal-Assisted Chemical Etching of Silicon in HF−H_2O_2. *Electrochim. Acta* **2008,** *53*, 5509–5516.
38. Cullis, A. G.; Canham, L. T.; Calcott, P. D. The Structural and Luminescence Properties of Porous Silicon. *J. Appl. Phys.* **1997,** *82*, 909–965.
39. Tsujino, K.; Matsumura, M. Helical Nanoholes Bored in Silicon by Wet Chemical Etching Using Platinum Nanoparticles as Catalyst. *Electrochem. Solid-State Lett.* **2005,** *8*, C193–C195.
40. Goszner, K.; Bischof, H. The Decomposition of Hydrogen Peroxide on Silver−Gold Alloys. *J. Catal.* **1974,** *32*, 175–182.
41. Maluf, N.; Williams, K. *An Introduction to Microelectromechanical Systems Engineering*, 2nd ed.; Artech House, Inc.: Boston, MA, 2004.